Article

Composition Tunable Manganese Ferrite Nanoparticles for Optimized T2 Contrast Ability

Lijiao Yang, Lengceng Ma, Jingyu Xin, Ao Li, Chengjie Sun, Ruixue Wei, Bin W. Ren, Zhong Chen, Hongyu Lin, and Jinhao Gao

Chem. Mater., **Just Accepted Manuscript** • DOI: 10.1021/acs.chemmater.7b00035 • Publication Date (Web): 16 Mar 2017

Composition Tunable Manganese Ferrite Nanoparticles for Optimized T_2 Contrast Ability

Lijiao Yang[1], Lengceng Ma[2], Jingyu Xin[1], Ao Li[1], Chengjie Sun[1], Ruixue Wei[1], Bin W. Ren[1], Zhong Chen[2], Hongyu Lin[1], and Jinhao Gao[1]*

[1]State Key Laboratory of Physical Chemistry of Solid Surfaces, The MOE Key Laboratory of Spectrochemical Analysis & Instrumentation, The Key Laboratory for Chemical Biology of Fujian Province, and iChEM, College of Chemistry and Chemical Engineering, Xiamen University, Xiamen 361005, China.

[2]Department of Electronic Science, Fujian Key Laboratory of Plasma and Magnetic Resonance, College of Physical Science and Technology, Xiamen University, Xiamen, 361005, China

*Email: jhgao@xmu.edu.cn

ABSTRCT

Manganese-doped magnetite nanoparticles as magnetic resonance imaging (MRI) contrast agents have been well developed in recent years due to their higher saturation magnetization and stronger transverse (T_2) contrast ability compared to parent magnetite. However, the underlying role that manganese doping plays in altering the contrast ability of magnetite is still not thoroughly understood. Herein, we investigate the effects of manganese doping on changes of ferrite crystal structures, magnetic properties, and contrast abilities. We developed a successful one-pot synthesis of uniform manganese-doped magnetite ($Mn_xFe_{3-x}O_4$) nanoparticles with different manganese contents (x = 0 ~ 1.06). The saturation magnetization and T_2 contrast ability of ferrite nanoparticles increase along with rising manganese proportion, peak when the doping level of $Mn_xFe_{3-x}O_4$ reaches x = 0.43, while decrease dramatically as the manganese percentage continues to augment. At high manganese doping level, the manganese ferrite nanoparticles may undergo lattice distortion according to analysis of XRD patterns and lattice distances, which may result in low saturation magnetization and eventually low T_2 contrast ability. The $Mn_xFe_{3-x}O_4$ nanoparticles (x = 0.43) with a diameter of ~18.5 nm exhibit the highest T_2 relaxivity of 904.4 $mM^{-1}s^{-1}$ at 7.0 T among all the samples, and show a much stronger T_2 contrast effect for liver imaging than other iron oxide contrast agents. These results indicate that the optimized T_2 contrast ability of manganese ferrite nanoparticles could be achieved by tuning the manganese doping level. This work also opens a new field of vision for developing high-performance T_2 contrast agents by modulating the metal composition of nanoparticles.

INTRODUCTION

Magnetite nanoparticles as T_2 magnetic resonance imaging (MRI) contrast agents (CAs) have been well-established over the past two decades,[1-4] but its low signal sensitivity is a major limitation and still not able to meet clinical needs in diagnosis and therapy.[5-7] Researchers have exploited a series of methods to enhance their contrast abilities in MRI, such as tuning their morphologies and compositions.[8-11] This strategy has been used for metal doping ferrite MFe_2O_4 (M = Fe, Co, Ni, and Mn) nanoparticles as well.[12-14] In Fe_3O_4 inverse spinel structure, oxide anions form face-centered cubic framework, while iron cations occupy part of the interstitial octahedral (O_h) and tetrahedral (T_d) sites.[15] Fe^{3+} cations in T_d and O_h sites are antiferromagnetic coupling, which leads to cancellation of magnetic moments. Consequently, the final magnetic moment of Fe_3O_4 unit proves to be the net magnetic moment of Fe^{2+} cation.[16] By replacing Fe^{2+} (d_6) with Mn^{2+} (d_5), Co^{2+} (d_7), or Ni^{2+} (d_8), the net magnetic moment of MFe_2O_4 unit can be engineered from 4 μ_B to 5 μ_B, 3 μ_B, or 2 μ_B, respectively.[13] Accordingly, the magnetic properties of MFe_2O_4 nanoparticles could also be tuned via replacing Fe^{2+} with other metal cations fully or partially.

Magnetic properties of nanoparticles are crucial for their performance in contrast-enhanced MRI.[17-19] According to quantum mechanical outer sphere theory, T_2 contrast enhancement is mainly related to the proton's effective diffusion and interaction with the magnetic dipolar moment: $r_2 = (256\pi^2\gamma^2/405)\ V^* M_s^2\ r^2/\ D\ (1+L/a)$, where M_s is saturation magnetization and r is effective radius of magnetic nanostructure, D is the diffusivity of water molecules, L is the thickness of an impermeable surface coating, and V^* is the volume fraction, respectively.[20-22] Nanoparticles with higher M_s values generate stronger local magnetic field inhomogeneity for the water proton dephasing process around themselves, which accelerates transverse (T_2) relaxation of water protons.[23] Thus their r_2 values are

highly dependent on their magnetic saturation magnetization. Types and amounts of metal dopants play a significant role in the magnetic properties of ferrite nanoparticles,[24-25] which can eventually alter T_2 contrast ability. The doping level of metal also has a great effect on crystal structures of ferrite nanoparticles. For example, Zn^{2+} ions doping converts the inverse spinel structure of Fe_3O_4 to the spinel structure of $(Zn_xFe_{1-x})Fe_2O_4$ according to the extended X-ray absorption fine structure (EXAFS) analysis.[9] Therefore, the influence of metal dopants on crystal structure and contrast ability of MFe_2O_4 nanoparticles needs to be taken into account for the development of nanoparticle-based T_2 CAs.

Among the previously discussed nanoparticles, manganese-doped magnetite nanoparticles have the highest magnetic susceptibility owning to the presence of five single unpaired electrons of Mn^{2+}. Besides, the net magnetic moment of $MnFe_2O_4$ unit is 5 μ_B not matter whether Mn(II) ions occupy octahedral or tetrahedral sites in the spinel structure of magnetite. As one of the most promising T_2 MRI contrast agents in theory, the manganese-doped magnetite nanoparticle-based CAs have been developed in recent years.[26-31] Nevertheless, the investigation on the mechanism of the underlying role that manganese plays in magnetic properties and contrast abilities of magnetite is neglected. Hence the relationships among manganese doping levels, crystal structures, magnetic properties, and T_2 contrast abilities need to be further clarified.

In this work, we synthesized manganese-doped magnetite ($Mn_xFe_{3-x}O_4$) nanoparticles with varied doping levels using a facile method and investigated their crystal structures, magnetic properties and contrast abilities. We found that lattice distances and saturation magnetizations of $Mn_xFe_{3-x}O_4$ are enlarged gradually with manganese doping level increasing. When the ratio of Mn/Fe reaches to 1/7 ($x = 0.43$), $Mn_xFe_{3-x}O_4$ nanoparticles maintained a typical ferrite structure with ultrahigh saturation

magnetization (M_s) of 89.5 emu/g, which endows them with an extremely strong T_2 contrast effect with an r_2 value of 904.4 $mM^{-1}s^{-1}$ at 7.0 T. When the doping amount of manganese continues to increase, the crystal structure of $Mn_xFe_{3-x}O_4$ is distorted and the M_s value of nanoparticles decreased, resulting in diminishing r_2 values. The $Mn_xFe_{3-x}O_4$ nanoparticles (x = 0.43) with high-performance T_2 contrast ability provides much higher signal sensitivity for imaging of living subjects compared with other iron-oxide-based CAs.

EXPERIMENTAL SECTIONS

Materials. 1-octadecene (tech, 90%) were purchased from Acros Organics. Oleic acid (tech, 90%), manganese chloride tetrahydrate (99%) were purchased from Alfa Aesar. Iron (III) chloride anhydrous (>97%), sodium oleate, trisodium citrate dehydrate, hexane, and ethanol were purchased from Sinopharm Chemical Reagent Co. Ltd. (Shanghai, China). All chemicals were used as received without further purification.

Characterization. Transmission electron microscopy images (TEM) and high-resolution TEM (HRTEM) were obtained by JEOL JEM-2100 microscope with an accelerating voltage of 200 kV. The X-ray powder diffraction (XRD) patterns of the nanoparticles were acquired on a Rigaku Ultima IV system (with Cu-Kα radiation, 30mA, 40 kV, scan angle (20°-70°), Sampling .W = 0.02, DivSlit (1/2 Deg), Div. HL. Slit = 10 mm). The energy-dispersive X-ray (EDX) element mapping was performed on a Tecnai F30 microscope at 300 kV. The X-ray absorption spectra were recorded at beamline BL14W1 of Shanghai Synchrotron Radiation Facility (SSRF, at Shanghai, China). The hysteresis loops (M-H curves at 300 K) were performed by the superconducting quantum interference device (SQUID). The hydrodynamic diameters of nanoparticles were measured with the

dynamic light scattering (DLS) measurements (Malvern Zetasizer nano ZS instrument). The metal concentration of the samples was measured with inductively coupled plasma atomic emission spectroscopy (ICP-AES).

Synthesis of iron oleate and manganese oleate complex. A metal oleate complex was carried out by reacting sodium oleate and metal chlorides according to a reported method with minor modification. In a typical experiment, 0.811 g of iron chloride (5 mmol) and 4.567 g of sodium oleate (15 mmol) were dissolved in a mixture of 20 mL ethanol, 15 mL distilled water and 30 mL hexane. The resulting solution was heated to 70 °C and stirred at that temperature for 4 h. After cooling to room temperature, the upper layer containing iron oleate was washed three times with distilled water. The resulting red brownish iron oleate complex in a waxy solid form was obtained after hexane was volatilized naturally in the dish. The manganese oleate complex (pink waxy solid) was prepared in a similar way except using manganese chloride as precursors and reacting under N_2 atmosphere. Then the manganese oleate complex was dissolved in ODE and sealed for further use.

Synthesis of Fe_3O_4 and $Mn_xFe_{3-x}O_4$ nanoparticles. A one-pot synthetic route of $Mn_xFe_{3-x}O_4$ nanoparticles (using x = 0.43 as example) is as follows: 0.903 g (1 mmol) of iron oleate (synthesized in a typical method) and 0.104 g (0.167 mmol) manganese oleate were dissolved in 15mL of 1-octadecene, with the addition of 0.186 mL (0.584 mmol) of oleic acid. The solution was first kept at 120 °C for 30 min in vacuum to remove air and other impurities then refluxed at 320 °C in N_2 for 2 h before cooling to room temperature. The products were separated by centrifugation, washed three times with ethanol, and dispersed in hexane for further use. The preparation of Fe_3O_4 nanoparticles is similar to the procedure without the adding of manganese oleate.

Transfer Fe_3O_4 and $Mn_xFe_{3-x}O_4$ nanoparticles into water. Briefly, sodium citrate in water and the as-prepared nanoparticles in hexane were mixed with the adding of acetone to initiate a ligand-exchange process. The $Mn_xFe_{3-x}O_4$ nanoparticles were gradually transferred to aqueous media by replacing oleic acid with sodium citrate, due to the fact that the chelation capability of the citrate to the nanoparticles surface is stronger than that of the original carboxyl groups of oleic acid. The sodium citrate-coated Fe_3O_4 nanoparticles were obtained with similar procedures.

Cytotoxicity Assay. The cytotoxicity of sodium citrate-coated $Mn_xFe_{3-x}O_4$ nanoparticles (x = 0.09, 0.43 and 1.06) was assessed by 3-(4,5-dimethylthiazol-2-y1)-2,5-diphenyltetrazolium bromide (MTT) assay using SMMC-7721 cells. Cells were firstly seeded into a 96-well plate with a density of 1×10^4 cells/well in RPMI 1640/ DMEM, and incubated under 5% CO_2 at 37 °C overnight. The cells were then incubated with the sodium citrate-coated $Mn_xFe_{3-x}O_4$ nanoparticles (x = 0.09, 0.43 and 1.06) at different [Mn + Fe] concentrations (0.469, 0.938, 1.875, 3.75, 7.5, 15, 30, 60 and 120 μg/mL) for 24 h. Then 100 μL of new culture media containing MTT (0.5 μg/mL) was added to each well and the cells were further incubated at 37 °C for 4 h. The OD_{492} value (Abs.) of each well was measured using a MultiSkan FC microplate reader immediately. Cell viability was calculated from OD_{492} values.

Cell uptake study. The SMMC-7721 cells (1×10^6) were seeded in dishes for 12 h, washed twice with PBS and incubated with 10 mL of RPMI 1640 containing $Mn_xFe_{3-x}O_4$ nanoparticles (x = 0.43) with different concentrations at 37 °C for 5 h. After harvesting the cells and washing them with PBS buffer for three times, we transferred the cells into 0.6 mL graduated centrifuge tubes and collected MR images on a 0.5 T MR scanner. We calculated the SNR by the equation: $SNR = SI/SD_{noise}$, where

SI represents signal intensity and SD represents standard deviation. The SNR changes were calculated by the equation: $SNR = |SNR_{post} - SNR_{pre}|/SNR_{pre}$.

Relaxivity and *in vitro* MRI phantom studies. The samples were firstly scanned using 0.5 T NMI20-Analyst NMR system. T_1- and T_2-weighted phantom images were acquired by a 2D multi-slice spin-echo (MSE) sequence: TR/TE = 200/2 ms (T_1), TR/TE = 2000/40 ms (T_2), 512 × 512 matrices. The relaxivities and MRI phantom images at 1.5 T were recorded by HT-MICNMR-60 system. T_1- and T_2-weighted phantom images were acquired by a spin-echo (SE) sequence: TR/TE = 100/8.3 ms (T_1), TR/TE = 5000/37 ms (T_2), 128 × 128 matrices, thickness = 0.8 mm, slice = 1. The relaxivities and MRI phantom images at 7 T (Varian 7T micro MRI) were recorded using a T_2-weighted fast spin-echo multi-slice sequence (fSEMS) (TR/TE = 2500/40 ms, FOV = 80 × 80 mm, thickness = 2 mm, slice = 1).

***In vivo* liver MRI.** *In vivo* MR imaging of liver was performed with BALB/c mice as a model. All animal experiments were carried out according to the protocol approved by Institutional Animal Care and Use Committee of Xiamen University. After intravenous injection of Fe_3O_4, $Mn_xFe_{3-x}O_4$ (x = 0.43 and x =1.06) and Feraheme at a dose of 1 mg Fe/kg of mouse body weight, we obtained the coronal and transverse plane MR images using an fSEMS sequence. The parameters are: TR/TE = 2500/32.8 ms, thickness = 1 mm, averages = 4, FOV = 40 × 40 mm (transverse plane) and FOV = 40 × 40 mm (coronal plane) on a Varian 7T micro MRI scanner.

RESULTS AND DISCUSSION

Synthesis and characterization. We used a simple and straightforward method to fabricate

$Mn_xFe_{3-x}O_4$ nanoparticles by thermal decomposition of iron oleate and manganese oleate as precursors and oleic acid as surfactant in 1-octadecene. We produced $Mn_xFe_{3-x}O_4$ nanoparticles (x from 0.09 to 1.06) with different manganese contents by tuning the ratios of two precursors and prepared Fe_3O_4 nanoparticles of similar size. Transmission electron microscopy (TEM) images (Figure 1) show that the as-synthesized $Mn_xFe_{3-x}O_4$ nanoparticles are of uniform spherical shape and narrow size distribution (about 18.5 nm in diameter, see Figure S1). We chose $Mn_xFe_{3-x}O_4$ nanoparticles (x = 0.43) to further characterize their structure. TEM images show they are uniform and high resolution TEM (HRTEM) images reveal good crystallinity with a lattice spacing distance of 0.30 nm (Figure 2a), which corresponds to (220) planes of inverse spinel magnetite. Selected area electron diffraction (SAED) also shows a crystalline nature of magnetite (Figure 2b). As shown in X-ray photoelectron spectroscopy (XPS) spectra (Figure S2), the peaks of 710.6 eV and 724.1 eV are assigned to Fe $2p_{3/2}$ and Fe $2p_{1/2}$ of magnetite,[32-33] while the peaks of 641.4 eV (Mn $2p_{3/2}$) and 653.1 eV (Mn $2p_{1/2}$) indicate the oxidation state of Mn(II).[34-35] The energy-dispersive X-ray line scanning analysis (EDX) (Figure 2c) and element mapping (Figure 2d) suggest that Mn(II) ions are homogeneously distributed in iron oxide nanoparticles.

Structures and properties. X-ray diffraction (XRD) patterns of $Mn_xFe_{3-x}O_4$ nanoparticles (Figure 3) show the diffraction peaks of inverse spinel structures of magnetite (JCPDS no. 01-089-0691). However, we found that all the peaks had varying degrees of shift compared to those of magnetite. The peak of (220) gradually shifted from 30.3 (x = 0) to 29.2 (x = 1.06). Similarly, the peak of (300) shifted from 35.5 to 34.7, (400) shifted from 42.9 to 42.0, (511) shifted from 57.0 to 56.2, and (440) shifted from 62.5 to 61.4. The shifting distances of the peaks are not the same, indicating that the shifts are not caused by baseline drift during data collection. It is probably due to the doping of

Mn(II) ions which partially change the structure of iron oxides. Since the radius of Mn(II) ions (67 pm) is larger than those of Fe(II) ions (61 pm) and Fe(III) ions (55 pm), Mn(II) ions occupying either octahedral or tetrahedral interstitial sites in the inverse spinel structure of magnetite may cause lattice distance bigger than that of pure magnetite. According to Bragg's law $n\lambda = 2d\sin\theta$, since λ is a constant determined by Cu-Kα radiation and n is the same, θ would diminish as d increases, in other words, the peaks of $Mn_xFe_{3-x}O_4$ nanoparticles in XRD patterns should display left shifting. This phenomenon is further confirmed by the analysis of HRTEM images of $Mn_xFe_{3-x}O_4$ nanoparticles with different manganese doping levels (Figure 4). The distances of crystal lattice are increased from 0.29 nm (x = 0, Fe_3O_4) to 0.30 nm (x = 0.43, $Mn_xFe_{3-x}O_4$), and finally is 0.31 nm (x = 1.06, $Mn_xFe_{3-x}O_4$). To analyze the tiny but significant change, we also measured the lattice distance of these nanoparticles by counting a large number of HRTEM images to make an average (the method and the details are showed in Table S1). This result indicates that the lattice distance gradually increases as manganese doping level is elevated. The calculated spacing from XRD analysis is close to the lattice distance obtained from HRTEM images, confirming the augment tendency of lattice distance as manganese doping level increases. It is also noteworthy that when the doping level is less than 0.43, the peaks in XRD show small shifts compared to those of Fe_3O_4, while the peaks shift significantly when the doping level is higher than 0.47. This result indicates that high doping level of manganese would disturb the original structure of $Mn_xFe_{3-x}O_4$ greatly. Meanwhile, the lattice fringes become unclear and disturbed when manganese doping level is higher than 0.47, finally the lattice fringe is considerably distorted in the case of x = 1.06. All these results indicate that as manganese doping level increases, the crystal structure change of $Mn_xFe_{3-x}O_4$ nanoparticles becomes significant, which is reflected by the increment in lattice distances and the disturbed lattice fringes.

Magnetic Properties. We measured the magnetic properties of $Mn_xFe_{3-x}O_4$ nanoparticles at a magnetic field of 5 T at 300 K. Field-dependent magnetization (*M*-*H*) curves (Figure 5a) indicate that $Mn_xFe_{3-x}O_4$ nanoparticles show different magnetic properties as manganese doping level changes. The coercivity in hysteresis loops is negligible at 300 K for all the samples. However, the $Mn_xFe_{3-x}O_4$ nanoparticles exhibit typical superparamagnetic behaviors when the manganese doping level is less than 0.61, while gradually become partially paramagnetic as the doping level increases. The magnetizations of the three samples (x = 0.79, 0.93, and 1.06) tend to be unsaturated even at the maximal applied magnetic field of 5 T, indicating that these three samples exhibit partially paramagnetic behaviors at room temperature. This is probably attributed to the doping manganese ions which disturb the long-range order of magnetic spins in magnetite and interrupt the magnetic dipolar coupling. The M_s values (Table S4) of $Mn_xFe_{3-x}O_4$ nanoparticles are 50.8, 60.1, 67.7, 73.3, 83.9, 89.5, 75.6, 69.9, 60.9, 44.0, 35.2 and 21.1 emu/g (emu/mass of Fe and O atoms in total) for x from 0 (Fe_3O_4) to 1.06, respectively. The M_s increases from 50.8 emu/g to 89.5 emu/g as manganese doping level rises from x = 0 to x = 0.43 (Figure 5b). This is because Mn(II) ions have five single electrons, which is the same as Fe(III) ions, and one more than Fe(II) ions. With an external magnetic field, the magnetic spins in O_h sites align parallel and those in T_d sites align antiparallel with the direction of the external magnetic field.[13] Therefore, with the assumption that Mn ions prefer T_d sites, the net magnetic spins of $Mn_xFe_{3-x}O_4$ unit is calculated to be (4+x) μ_B (for x>1, it is always 5 μ_B), higher than that of Fe_3O_4 unit with 4 μ_B, which explains that magnetic susceptibility of $Mn_xFe_{3-x}O_4$ is enhanced as manganese doping level increases. However, as the doping level further augments, the M_s shows a stepwise decrease to 21.1 emu/g (x = 1.06), which may be due to the fact that the crystal structure is disturbed severely by a large amount of manganese doping. According to

XRD patterns and lattice distances analysis, manganese ferrite nanoparticles undergo lattice distortion at high manganese doping level, which interrupts the magnetic dipolar coupling and results in low saturation magnetization.

Relaxivity Measurements. Coating methods have been well developed in recent years for magnetic nanoparticles as contrast agents.[36-38] To achieve good biocompatibility, we coated Fe_3O_4 and $Mn_xFe_{3-x}O_4$ nanoparticles with sodium citrate to confer water solubility. We chose sodium citrate but not macromolecules (for example, PEG and PVP with large volume) because sodium citrate coating would not change the diameter of nanoparticles significantly. Researches have already showed that nanoparticles smaller than 50 nm can escape phagocytosis to some extent, resulting in a prolonged circulation time,[39-41] therefore maintaining the small size of nanoparticles would be beneficial for biomedical applications. Dynamic light scattering (DLS) analysis (Figure S3 and Table S3) indicates that Fe_3O_4 and $Mn_xFe_{3-x}O_4$ nanoparticles are very stable with narrow size distribution in water. Moreover, there is little change in the diameter between the as-prepared nanoparticles and the nanoparticles after coating with sodium citrate.

We then studied the contrast enhancement abilities of $Mn_xFe_{3-x}O_4$ nanoparticles with different manganese doping levels. We firstly performed the relaxivity test on a 0.5 T MRI scanner. It is noteworthy that both the T_1 and T_2 relaxivities showed interesting trends as the manganese doping level increases. The r_2 values (Figure 6a and Table S4) are 128.3 ± 2.9 $mM^{-1}s^{-1}$ for Fe_3O_4 (x = 0, with respect to iron concentration), and 206.9 ± 1.9, 269.3 ± 6.0, 375.9 ± 14.1, 459.5 ± 5.7, 506.6 ± 18.7, 396.7 ± 11.5, 312.1 ± 14.8, 244.4 ± 2.6, 154.4 ± 1.2, 117.3 ± 0.6, 77.7 ± 2.4 $mM^{-1}s^{-1}$ (with respect to total metal ion concentration) for $Mn_xFe_{3-x}O_4$ nanoparticles (from x = 0.09 to x = 1.06), respectively. The highest r_2 value is 506.6 ± 18.7 $mM^{-1}s^{-1}$ when x = 0.43, 4 times higher than that of Fe_3O_4 and 6.5

times higher than that of $Mn_xFe_{3-x}O_4$ nanoparticles (x = 1.06), which is mainly attributed to the largest saturation magnetization. According to quantum mechanical outer sphere theory, saturation magnetization plays an important role in transverse relaxation, and a larger M_s brings about a higher r_2. Therefore, T_2 contrast abilities of ferrite nanoparticles should show a similar trend to their saturation magnetizations, peaking at x =0.43, which is consistent with experimental results (Figure 5b and Figure 6b). We also performed phantom imaging analysis. In T_2-weighted MR images, the tissue with a short T_2 relaxation time appears dark. We can observe that with the increase of total metals concentrations, the signal intensity of T_2-weighted phantom images reduces gradually in all the samples (Figure 6c). The T_2 contrast effect is the strongest when manganese doping level is 0.43, weakened as the doping level is reduced to 0 or increased to 1.06 gradually, indicating that x = 0.43 is the optimal manganese doping level of $Mn_xFe_{3-x}O_4$ nanoparticles as T_2 CAs.

Meanwhile, we also evaluated T_1 contrast abilities of $Mn_xFe_{3-x}O_4$ nanoparticles at different manganese doping levels (Figure S4a,b). The r_1 values of Fe_3O_4 (x = 0) and $Mn_xFe_{3-x}O_4$ nanoparticles (from x = 0.09 to x = 1.06) at 0.5 T are 19.4 ± 0.1, 26.8 ± 0.2, 45.1 ± 0.6, 60.1 ± 0.5, 70.3 ± 0.6, 76.5 ± 1.1, 64.2 ± 0.2, 50.5 ± 0.8, 32.4 ± 0.7, 17.0 ± 0.3, 13.7 ± 0.9 and 9.4 ± 0.2 $mM^{-1}s^{-1}$, respectively (Table S5). They have the similar trend to r_2 values at 0.5 T. Indeed, superparamagnetic nanoparticles also can shorten T_1 relaxation process. The r_1 value increases with the manganese proportion (x less than 0.43) may be attributed to the increased surface Mn^{2+} ions of $Mn_xFe_{3-x}O_4$ nanoparticles. Mn^{2+} ion has more unpaired electrons and longer electronic relaxation time than Fe^{2+} ion[42-44] , therefore has higher r_1 value according to SBM theory.[45-47] The r_1 values reduced with higher manganese proportion might because that the disordered metal atoms on surface lead to an ineffective coordinating and chemical exchanging process of protons.[48-49] The phantom imaging

showed the interesting changes of T_1 contrast effects clearly (Figure S5). The value of r_2/r_1 is crucial to estimate whether the nanoparticles can serve as a T_1 or T_2 contrast agent.[50-53] High r_2/r_1 ratio (> 10) results in T_2- dominated contrast effect and the low ratio (< 5) leads to T_1- dominated contrast effect.[49, 53-56] For T_1-T_2 dual-mode contrast agents, the suitable r_2/r_1 value is about 5-10.[57-61] The r_2/r_1 ratios of Fe_3O_4 (x = 0) and $Mn_xFe_{3-x}O_4$ nanoparticles (from x = 0.09 to x = 1.06) at 0.5 T are 6.6, 7.7, 6.0, 6.3, 6.5, 6.6, 6.2, 5.6, 7.5, 9.1, 8.6, and 8.3, respectively (see Table S5). The moderate r_2/r_1 values and high r_1 values of $Mn_xFe_{3-x}O_4$ nanoparticles (from x = 0.19 to x = 0.53) suggest that they can serve as T_1-T_2 dual-mode contrast agents in MRI with low magnetic fields (e.g., 0.5 T). Our results are also in agreement with this trend in the T_1- and T_2- weighted phantom imaging (Figure S5 and Figure 6c).

In theory, signal-to-noise ratio (SNR) is proportional to the square of external magnetic field while noise is directly proportional to external magnetic field, which means that the sensitivity of MR imaging can be enhanced by applying high magnetic field.[62] Taking this factor into account, we also conducted T_1 and T_2 relaxivity tests on a 7.0 T MRI scanner (Figure 7). Consistent with the situation at 0.5 T, the r_2 values are 244.2 ± 12.3, 397.1 ± 18.3, 512.5 ± 21.7, 715.6 ± 17.4, 855.3 ± 3.4, 904.4 ± 11.1, 748.4 ± 7.5, 591.3 ± 6.2, 460.0 ± 5.3, 289.5 ± 1.2, 236.4 ± 12.4, and 139.1 ± 1.7 mM^{-1} s^{-1} for Fe_3O_4 (x = 0) and $Mn_xFe_{3-x}O_4$ nanoparticles (from x = 0.09 to 1.06), respectively, peaking at x = 0.43 (Figure 7a and Table S4). The strength of magnetic field is an important parameter for the relaxivities of magnetic nanoparticles.[63] The r_2 values of the nanoparticles are greatly increased, while the r_1 values are significantly diminished at a high magnetic field.[63-64] The r_1 values (Figure S4c,d) are 1.46 ± 0.02, 1.21 ± 0.13, 0.90 ± 0.05, 0.73 ± 0.01, 0.56 ± 0.01, 0.50 ± 0.01, 0.76 ± 0.02, 0.87 ± 0.05, 1.19 ± 0.02, 1.73 ± 0.09, 1.90 ± 0.11, and 2.19 ± 0.04 mM^{-1} s^{-1} for Fe_3O_4 (x = 0) and

$Mn_xFe_{3-x}O_4$ nanoparticles (from x = 0.09 to 1.06), and the r_2/r_1 ratios are about 165, 328, 569, 980, 1527, 1809, 985, 680, 387, 167, 124, 64, respectively (Table S5). The ultrahigh r_2/r_1 values suggest that $Mn_xFe_{3-x}O_4$ nanoparticles only serve as T_2 contrast agents at high fields. It is noteworthy that $Mn_xFe_{3-x}O_4$ nanoparticles (x = 0.43) exhibits the highest negative contrast effect (Figure 7b) with a r_2 value of 904.4 $mM^{-1}s^{-1}$, which is the highest r_2 value ever reported to the best of our knowledge, and is about 9.2 times higher than that of Feraheme (ferumoxytol, iron oxide nanoparticles with a r_2 value of 98.4 $mM^{-1}s^{-1}$ at 7.0 T, see Figure S6), an approved MRI contrast agent in clinical practice. The ultrahigh transverse relaxivity leads to a strong T_2 contrast effect in MR imaging. As shown in Figure 7c, compared to the signal of water, a significant dark signal for $Mn_xFe_{3-x}O_4$ (x = 0.43) was observed even when the concentration of total metal was only 0.05 mM^{-1}, indicating that these nanoparticles hold great promise for highly sensitive and accurate detection in imaging and diagnosis. We also performed the longitudinal and transverse relaxivities of $Mn_xFe_{3-x}O_4$ (x = 0.43) nanoparticles at clinical field strengths. The r_1 and r_2 values of $Mn_xFe_{3-x}O_4$ (x = 0.43) nanoparticles are 737.2 ± 16.7 and 19.93 ± 0.17 mM^{-1} s^{-1} at 1.5 T, respectively, indicating that $Mn_xFe_{3-x}O_4$ (x = 0.43) nanoparticles can serve as excellent T_2 contrast agents at clinical field strengths.

***In vitro* and *in vivo* MRI studies.** Before *in vivo* studies, we first evaluated the cytotoxicity of sodium citrate-coated $Mn_xFe_{3-x}O_4$ nanoparticles (x = 0.09, 0.43, and 1.06) using SMMC-7721 cells as a model by tetrazolium-based colorimetric (MTT) assays. They showed no appreciable cytotoxicity even at high concentrations (up to 120 μg [Mn + Fe] mL^{-1}) after 24 hour incubation of SMMC-7721 cells, suggesting the good biocompatibility of the water-dispersible $Mn_xFe_{3-x}O_4$ nanoparticles (Figure S8). Moreover, the particle size changed little after incubation with fetal bovine serum (FBS), suggesting the good stability of these nanoparticles in the presence of serum

proteins (Figure S9). We also tested the T_1- and T_2- weighted MRI contrast abilities of $Mn_xFe_{3-x}O_4$ nanoparticles (x = 0.43) *in vitro* by incubating SMMC-7721 cells with them at different concentrations (0.2, 0.4, and 0.8 mM [Mn + Fe]) on a 0.5 T MR scanner (Figure S10 and Table S7). Cells after being incubated with $Mn_xFe_{3-x}O_4$ nanoparticles at higher concentration showed brighter signals in T_1 imaging and darker signals in T_2 imaging. SNR changes ΔSNR (ΔSNR = $|SNR_{post} - SNR_{pre}|/SNR_{pre}$) for cells (Table S8) incubated with $Mn_xFe_{3-x}O_4$ nanoparticles at the concentration of 0.8 mM are 60.5 ± 4.31% in T_1 images and 76.1 ± 1.7% in T_2 images, demonstrating that $Mn_xFe_{3-x}O_4$ nanoparticles show both T_1 and T_2 MR contrast enhancement effects *in vitro* at a low magnetic field of 0.5T.

To evaluate the contrast abilities of $Mn_xFe_{3-x}O_4$ nanoparticles *in vivo*, we chose Fe_3O_4 (x = 0) nanoparticles, $Mn_xFe_{3-x}O_4$ nanoparticles (x = 0.43 and x = 1.06) as the representative samples, and used Feraheme as control. Nanoparticles are rapidly taken up by mononuclear phagocyte system (MPS) and easily accumulated in hepatic Kupffer cells in liver,[65-67] so we focused on liver as the region of interest (ROI). We used healthy BALB/c mice as the model to conduct the animal experiments and perform T_2- weighted MRI of liver. After intravenous injection of these four samples at a dose of only 1 mg [Fe]/kg or 1 mg [Mn + Fe]/kg mouse body weight, we observed significant signal attenuation for four groups at 0.5, 1, 2, and 4 h post injection (p.i.) of transverse plane (Figure 8a) and coronal plane (Figure S11a) in the liver region. The liver region became dark at 0.5 h post-injection, reached maximum dark signals at 2 h and showed brighter signals at 4 h than those at 2 h. The bright signals at 4 h (also can be confirmed in Table S9 and Table S10 SNR changes) imply that the nanoparticles started to degrade and were excreted from the body. Previous studies reported the way taken by cells *in vivo* to process and degrade iron oxide nanoparticles over

time.[68-70] Moreover, size plays a strong role in biodistribution and blood circulation, the 18 nm-sized particles we used have numerous benefits for *in vivo* applications.[71-72] Smaller particles (<10 nm) reach various organs by crossing the tight endothelial junctions and are rapidly excreted through the glomeruli of the kidneys.[73-74]

Especially for $Mn_xFe_{3-x}O_4$ (x = 0.43), the liver region showed obvious dark signals only at 0.5 h and reached maximum dark signals at 2 h post-injection. These results demonstrate that $Mn_xFe_{3-x}O_4$ nanoparticles have a fast contrast-enhanced effect and relative long diagnostic time window for several hours after intravenous administration, which could provide more useful information for diagnosis with enhanced accuracy.

To quantitate the different contrast abilities of four samples, we analyzed the SNR_{post}/SNR_{pre} value for each animal of transverse plane (Figure 8b) and coronal plane (Figure S11b). The SNR (%) of Fe_3O_4, $Mn_xFe_{3-x}O_4$ (x = 0.43), $Mn_xFe_{3-x}O_4$ (x =1.06) and Feraheme at 2 h for transverse plane are 71.7 ± 1.9, 19.0 ± 1.3, 85.0 ± 1.9, 91.8 ± 1.9, respectively. The $Mn_xFe_{3-x}O_4$ nanoparticles (x = 0.43) exhibited the best enhancement effects and the maximal ΔSNR was up to 81.0 ± 1.3% for transverse plane (Table S9, coronal plane see Table S10), ~2.9 times higher than that of Fe_3O_4, ~5.4 times higher than that of $Mn_xFe_{3-x}O_4$ (x = 1.06), and ~9.9 times higher than that of Feraheme. These results suggest that $Mn_xFe_{3-x}O_4$ nanoparticles (x = 0.43) with an ultrahigh r_2 value hold great promise as an excellent T_2 contrast agent for sensitive imaging and diagnosis. On the other hand, the high contrast ability of $Mn_xFe_{3-x}O_4$ nanoparticles (x = 0.43) indicates a low injection dose, which may imply lower cost, less side effects, and better potential for clinical translation.

CONCLUSIONS

In summary, we introduced a facile method to produce a series of manganese doping magnetite nanoparticles by one-pot synthesis. By tuning the manganese doping level and investigating the changes in crystal structures and magnetic properties, we uncovered the possible role of manganese ions in altering magnetite structures and contrast abilities. It is demonstrated that saturation magnetizations (M_s) and T_2 relaxivities of $Mn_xFe_{3-x}O_4$ nanoparticles increase as the manganese doping level rises, reach the maximum when x = 0.43, and decrease as the manganese doping level continues to augment. The optimized manganese ferrite nanoparticles with ultrahigh T_2 contrast ability show a great potential in sensitive imaging and diagnosis. This work provides a strategy to develop high-performance negative contrast agents by tuning metal composition of nanoparticles. Furthermore, besides morphology, size, and surface structure,[8, 33, 49] composition of iron-oxide-based nanoparticles should be also carefully considered for design of new-generation T_2 contrast agents.

ASSOCIATED CONTENT

Supporting Information

The Figures S1-S11 and Tables S1-S10. This material is available free of charge *via* the Internet at http://pubs.acs.org.

AUTHOR INFORMATION

Corresponding Author

*Email: jhgao@xmu.edu.cn

Notes

The authors declare no competing financial interests.

Acknowledgements

This work was supported by National Natural Science Foundation of China (81370042, 81430041, 21602186, and 21521004), National Key Basic Research Program of China (2013CB933901, 2014CB744502, and 2014CB932004), Fundamental Research Funds for the Central Universities (20720160074), and Department of Human Resources of Fujian Province.

REFERENCES

(1) Zhou, Z.; Zhu, X.; Wu, D.; Chen, Q.; Huang, D.; Sun, C.; Xin, J.; Ni, K.; Gao, J., Anisotropic Shaped Iron Oxide Nanostructures: Controlled Synthesis and Proton Relaxation Shortening Effects. *Chem. Mater.* **2015,** *27*, 3505-3515.

(2) Wu, L.; Mendoza-Garcia, A.; Li, Q.; Sun, S., Organic Phase Syntheses of Magnetic Nanoparticles and Their Applications. *Chem. Rev.* **2016,** *116*, 10473-512.

(3) Casula, M. F.; Floris, P.; Innocenti, C.; Lascialfari, A.; Marinone, M.; Corti, M.; Sperling, R. A.; Parak, W. J.; Sangregorio, C., Magnetic Resonance Imaging Contrast Agents Based on Iron Oxide Superparamagnetic Ferrofluids. *Chem. Mater.* **2010,** *22*, 1739-1748.

(4) Tassa, C.; Shaw, S. Y.; Weissleder, R., Dextran-coated iron oxide nanoparticles: a versatile platform for targeted molecular imaging, molecular diagnostics, and therapy. *Acc. Chem. Res.* **2011,** *44*, 842-52.

(5) Poselt, E.; Kloust, H.; Tromsdorf, U.; Janschel, M.; Hahn, C.; Masslo, C.; Weller, H., Relaxivity optimization of a PEGylated iron-oxide-based negative magnetic resonance contrast agent for T(2)-weighted spin-echo imaging. *ACS Nano* **2012,** *6*, 1619-24.

(6) Ghosh, D.; Lee, Y.; Thomas, S.; Kohli, A. G.; Yun, D. S.; Belcher, A. M.; Kelly, K. A., M13-templated magnetic nanoparticles for targeted in vivo imaging of prostate cancer. *Nat. Nanotechnol.* **2012,** *7*, 677-82.

(7) Gao, J.; Gu, H.; Xu, B., Multifunctional magnetic nanoparticles: design, synthesis, and biomedical applications. *Acc. Chem. Res.* **2009,** *42*, 1097-107.

(8) Zhao, Z.; Chi, X.; Yang, L.; Yang, R.; Ren, B. W.; Zhu, X.; Zhang, P.; Gao, J., Cation Exchange of Anisotropic-Shaped Magnetite Nanoparticles Generates High-Relaxivity Contrast Agents for Liver Tumor Imaging. *Chem. Mater.* **2016,** *28*, 3497-3506.

(9) Jang, J. T.; Nah, H.; Lee, J. H.; Moon, S. H.; Kim, M. G.; Cheon, J., Critical enhancements of MRI contrast and hyperthermic effects by dopant-controlled magnetic nanoparticles. *Angew. Chem.* **2009,** *48*, 1234-8.

(10) Liu, Y.; Goebl, J.; Yin, Y., Templated synthesis of nanostructured materials. *Chem. Soc. Rev.* **2013,** *42*, 2610-53.

(11) Yang, L.; Zhou, Z.; Liu, H.; Wu, C.; Zhang, H.; Huang, G.; Ai, H.; Gao, J., Europium-engineered iron oxide nanocubes with high T1 and T2 contrast abilities for MRI in living subjects. *Nanoscale* **2015,** *7*, 6843-50.

(12) Yu, Y.; Mendoza-Garcia, A.; Ning, B.; Sun, S., Cobalt-substituted magnetite nanoparticles and their assembly into ferrimagnetic nanoparticle arrays. *Adv. Mater.* **2013,** *25*, 3090-4.

(13) Lee, J. H.; Huh, Y. M.; Jun, Y. W.; Seo, J. W.; Jang, J. T.; Song, H. T.; Kim, S.; Cho, E. J.; Yoon, H. G.; Suh, J. S.; Cheon, J., Artificially engineered magnetic nanoparticles for ultra-sensitive molecular imaging. *Nat. Med.* **2007,** *13*, 95-9.

(14) Colombo, M.; Carregal-Romero, S.; Casula, M. F.; Gutierrez, L.; Morales, M. P.; Bohm, I. B.; Heverhagen, J. T.; Prosperi, D.; Parak, W. J., Biological applications of magnetic nanoparticles. *Chem. Soc. Rev.* **2012,** *41*, 4306-34.

(15) Schultz-Sikma, E. A.; Joshi, H. M.; Ma, Q.; MacRenaris, K. W.; Eckermann, A. L.; Dravid, V. P.; Meade, T. J., Probing the Chemical Stability of Mixed Ferrites: Implications for Magnetic Resonance Contrast Agent Design. *Chem. Mater.* **2011,** *23*, 2657-2664.

(16) Lee, J.; Zhang, S.; Sun, S., High-Temperature Solution-Phase Syntheses of Metal-Oxide Nanocrystals. *Chem. Mater.* **2013,** *25*, 1293-1304.

(17) Qiao, R.; Jia, Q.; Huwel, S.; Xia, R.; Liu, T.; Gao, F.; Galla, H. J.; Gao, M., Receptor-mediated delivery of magnetic nanoparticles across the blood-brain barrier. *ACS Nano* **2012,** *6*, 3304-10.
(18) Jun, Y. W.; Seo, J. W.; Cheon, J., Nanoscaling laws of magnetic nanoparticles and their applicabilities in biomedical sciences. *Acc. Chem. Res.* **2008,** *41*, 179-89.
(19) Cheong, S.; Ferguson, P.; Feindel, K. W.; Hermans, I. F.; Callaghan, P. T.; Meyer, C.; Slocombe, A.; Su, C. H.; Cheng, F. Y.; Yeh, C. S.; Ingham, B.; Toney, M. F.; Tilley, R. D., Simple synthesis and functionalization of iron nanoparticles for magnetic resonance imaging. *Angew. Chem. Int. Ed. Engl.* **2011,** *50*, 4206-9.
(20) Koenig, S. H.; Kellar, K. E., Theory of 1/T1 and 1/T2 NMRD profiles of solutions of magnetic nanoparticles. *Magn. Reson. Med.* **1995,** *34*, 227-233.
(21) Gillis, P.; Moiny, F.; Brooks, R. A., On T(2)-shortening by strongly magnetized spheres: a partial refocusing model. *Magn. Reson. Med.* **2002,** *47*, 257-63.
(22) Brooks, R. A.; Moiny, F.; Gillis, P., On T2-shortening by weakly magnetized particles: the chemical exchange model. *Magn. Reson. Med.* **2001,** *45*, 1014-20.
(23) Vuong, Q. L.; Berret, J. F.; Fresnais, J.; Gossuin, Y.; Sandre, O., A universal scaling law to predict the efficiency of magnetic nanoparticles as MRI T(2)-contrast agents. *Adv. Healthcare Mater.* **2012,** *1*, 502-12.
(24) Sathya, A.; Guardia, P.; Brescia, R.; Silvestri, N.; Pugliese, G.; Nitti, S.; Manna, L.; Pellegrino, T., CoxFe3–xO4Nanocubes for Theranostic Applications: Effect of Cobalt Content and Particle Size. *Chem. Mater.* **2016,** *28*, 1769-1780.
(25) Beji, Z.; Hanini, A.; Smiri, L. S.; Gavard, J.; Kacem, K.; Villain, F.; Grenèche, J. M.; Chau, F.; Ammar, S., Magnetic properties of Zn-substituted MnFe2O4nanoparticles synthesized in polyol as potential heating agents for hyperthermia. Evaluation of their toxicity on Endothelial cells. *Chem. Mater.* **2010,** *22*, 5420-5429.
(26) Huang, G.; Li, H.; Chen, J.; Zhao, Z.; Yang, L.; Chi, X.; Chen, Z.; Wang, X.; Gao, J., Tunable T1 and T2 contrast abilities of manganese-engineered iron oxide nanoparticles through size control. *Nanoscale* **2014,** *6*, 10404-12.
(27) Song, Q.; Ding, Y.; Wang, Z. L.; Zhang, Z. J., Tuning the Thermal Stability of Molecular Precursors for the Nonhydrolytic Synthesis of Magnetic MnFe2O4Spinel Nanocrystals. *Chem. Mater.* **2007,** *19*, 4633-4638.
(28) Tromsdorf, U. I.; Bigall, N. C.; Kaul, M. G.; Bruns, O. T.; Nikolic, M. S.; Mollwitz, B.; Sperling, R. A.; Reimer, R.; Hohenberg, H.; Parak, W. J.; Forster, S.; Beisiegel, U.; Adam, G.; Weller, H., Size and surface effects on the MRI relaxivity of manganese ferrite nanoparticle contrast agents. *Nano Lett.* **2007,** *7*, 2422-7.
(29) Lu, J.; Ma, S.; Sun, J.; Xia, C.; Liu, C.; Wang, Z.; Zhao, X.; Gao, F.; Gong, Q.; Song, B.; Shuai, X.; Ai, H.; Gu, Z., Manganese ferrite nanoparticle micellar nanocomposites as MRI contrast agent for liver imaging. *Biomaterials* **2009,** *30*, 2919-28.
(30) Yang, H.; Zhang, C.; Shi, X.; Hu, H.; Du, X.; Fang, Y.; Ma, Y.; Wu, H.; Yang, S., Water-soluble superparamagnetic manganese ferrite nanoparticles for magnetic resonance imaging. *Biomaterials* **2010,** *31*, 3667-73.
(31) Liu, C.; Zhang, Z. J., Size-Dependent Superparamagnetic Properties of Mn Spinel Ferrite Nanoparticles Synthesized from Reverse Micelles. *Chem. Mater.* **2001,** *13*, 2092-2096.
(32) Yamashita, T.; Hayes, P., Analysis of XPS spectra of Fe2+ and Fe3+ ions in oxide materials. *Appl. Surf. Sci.* **2008,** *254*, 2441-2449.

(33)Zhao, Z.; Zhou, Z.; Bao, J.; Wang, Z.; Hu, J.; Chi, X.; Ni, K.; Wang, R.; Chen, X.; Chen, Z.; Gao, J., Octapod iron oxide nanoparticles as high-performance T(2) contrast agents for magnetic resonance imaging. *Nat. Commun.* **2013,** *4*, 2266.
(34)Tan, B. J.; Klabunde, K. J.; Sherwood, P. M. A., XPS studies of solvated metal atom dispersed (SMAD) catalysts. Evidence for layered cobalt-manganese particles on alumina and silica. *J. Am. Chem. Soc.* **1991,** *113*, 855-861.
(35)Xu, Y.; Sherwood, J.; Qin, Y.; Holler, R. A.; Bao, Y., A general approach to the synthesis and detailed characterization of magnetic ferrite nanocubes. *Nanoscale* **2015,** *7*, 12641-9.
(36)Tong, S.; Hou, S.; Zheng, Z.; Zhou, J.; Bao, G., Coating optimization of superparamagnetic iron oxide nanoparticles for high T2 relaxivity. *Nano Lett.* **2010,** *10*, 4607-13.
(37)Gallo, J.; Long, N. J.; Aboagye, E. O., Magnetic nanoparticles as contrast agents in the diagnosis and treatment of cancer. *Chem. Soc. Rev.* **2013,** *42*, 7816-33.
(38)Berry, C. C.; Wells, S.; Charles, S.; Aitchison, G.; Curtis, A. S. G., Cell response to dextran-derivatised iron oxide nanoparticles post internalisation. *Biomaterials* **2004,** *25*, 5405-5413.
(39)Wang, Y. X.; Hussain, S. M.; Krestin, G. P., Superparamagnetic iron oxide contrast agents: physicochemical characteristics and applications in MR imaging. *Eur. Radiol.* **2001,** *11*, 2319-31.
(40)Li, W.; Tutton, S.; Vu, A. T.; Pierchala, L.; Li, B. S.; Lewis, J. M.; Prasad, P. V.; Edelman, R. R., First-pass contrast-enhanced magnetic resonance angiography in humans using ferumoxytol, a novel ultrasmall superparamagnetic iron oxide (USPIO)-based blood pool agent. *J. Magn. Reson. Imaging* **2005,** *21*, 46-52.
(41)Chemistry of MaterialsChemistry of MaterialsPombo Garcia, K.; Zarschler, K.; Barbaro, L.; Barreto, J. A.; O'Malley, W.; Spiccia, L.; Stephan, H.; Graham, B., Zwitterionic-coated "stealth" nanoparticles for biomedical applications: recent advances in countering biomolecular corona formation and uptake by the mononuclear phagocyte system. *Small* **2014,** *10*, 2516-29.
(42)Lauffer, R. B., Paramagnetic metal complexes as water proton relaxation agents for NMR imaging: theory and design. *Chem. Rev.* **1987,** *87*, 901-927.
(43)Grant, M.; Jordan, R. B., Kinetics of solvent water exchange on iron(III). *Inorg. Chem.* **1981,** *20*, 55-60.
(44)Han, G.; Huang, Y.; Koua, F. H.; Shen, J. R.; Westlund, P. O.; Messinger, J., Hydration of the oxygen-evolving complex of photosystem II probed in the dark-stable S1 state using proton NMR dispersion profiles. *Phys. Chem. Chem. Phys.* **2014,** *16*, 11924-35.
(45)Zhang, M.; Cao, Y.; Wang, L.; Ma, Y.; Tu, X.; Zhang, Z., Manganese doped iron oxide theranostic nanoparticles for combined T1 magnetic resonance imaging and photothermal therapy. *ACS. Appl. Mater. Inter.* **2015,** *7*, 4650-8.
(46)Ananta, J. S.; Godin, B.; Sethi, R.; Moriggi, L.; Liu, X.; Serda, R. E.; Krishnamurthy, R.; Muthupillai, R.; Bolskar, R. D.; Helm, L.; Ferrari, M.; Wilson, L. J.; Decuzzi, P., Geometrical confinement of gadolinium-based contrast agents in nanoporous particles enhances T1 contrast. *Nat. Nanotechnol.* **2010,** *5*, 815-21.
(47)Westlund, P.-O.; Larsson, P. T.; Welinder, K. G.; Schneider, P.; Dunford, H. B.; Lahajnar, G.; Maartmann-Moe, K.; Karlsson, B., Proton-Enhanced Relaxation in Low-Symmetry Paramagnetic Complexes (S = 1): Beyond the Solomon--Bloembergen and Morgan Theory. 1. The Smoluchowsky Distortion Model of the ZFS Interaction. *Acta Chem. Scand.* **1991,** *45*, 11-18.
(48)Kim, B. H.; Lee, N.; Kim, H.; An, K.; Park, Y. I.; Choi, Y.; Shin, K.; Lee, Y.; Kwon, S. G.; Na, H. B.; Park, J. G.; Ahn, T. Y.; Kim, Y. W.; Moon, W. K.; Choi, S. H.; Hyeon, T., Large-scale synthesis of

uniform and extremely small-sized iron oxide nanoparticles for high-resolution T1 magnetic resonance imaging contrast agents. *J. Am. Chem. Soc.* **2011,** *133*, 12624-31.
(49) Zhou, Z.; Zhao, Z.; Zhang, H.; Wang, Z.; Chen, X.; Wang, R.; Chen, Z.; Gao, J., Interplay between Longitudinal and Transverse Contrasts in Fe3O4 Nanoplates with (111) Exposed Surfaces. *ACS Nano* **2014,** *8*, 7976-7985.
(50) Tromsdorf, U. I.; Bruns, O. T.; Salmen, S. C.; Beisiegel, U.; Weller, H., A Highly Effective, Nontoxic T1 MR Contrast Agent Based on Ultrasmall PEGylated Iron Oxide Nanoparticles. *Nano Lett.* **2009,** *9*, 4434-4440.
(51) Li, Z.; Wang, S. X.; Sun, Q.; Zhao, H. L.; Lei, H.; Lan, M. B.; Cheng, Z. X.; Wang, X. L.; Dou, S. X.; Lu, G. Q., Ultrasmall Manganese Ferrite Nanoparticles as Positive Contrast Agent for Magnetic Resonance Imaging. *Adv. Healthcare Mater.* **2013,** *2*, 958-964.
(52) Malyutin, A. G.; Easterday, R.; Lozovyy, Y.; Spilotros, A.; Cheng, H.; Sanchez-Felix, O. R.; Stein, B. D.; Morgan, D. G.; Svergun, D. I.; Dragnea, B.; Bronstein, L. M., Viruslike Nanoparticles with Maghemite Cores Allow for Enhanced MRI Contrast Agents. *Chem. Mater.* **2015,** *27*, 327-335.
(53) Dong, C.; Korinek, A.; Blasiak, B.; Tomanek, B.; van Veggel, F. C. J. M., Cation Exchange: A Facile Method To Make NaYF4:Yb,Tm-NaGdF4 Core–Shell Nanoparticles with a Thin, Tunable, and Uniform Shell. *Chem. Mater.* **2012,** *24*, 1297-1305.
(54) Zhou, Z.; Wang, L.; Chi, X.; Bao, J.; Yang, L.; Zhao, W.; Chen, Z.; Wang, X.; Chen, X.; Gao, J., Engineered Iron-Oxide-Based Nanoparticles as Enhanced T1 Contrast Agents for Efficient Tumor Imaging. *ACS Nano* **2013,** *7*, 3287-3296.
(55) Na, H. B.; Song, I. C.; Hyeon, T., Inorganic Nanoparticles for MRI Contrast Agents. *Adv. Mater.* **2009,** *21*, 2133-2148.
(56) Park, M.; Lee, N.; Choi, S. H.; An, K.; Yu, S.-H.; Kim, J. H.; Kwon, S.-H.; Kim, D.; Kim, H.; Baek, S.-I.; Ahn, T.-Y.; Park, O. K.; Son, J. S.; Sung, Y.-E.; Kim, Y.-W.; Wang, Z.; Pinna, N.; Hyeon, T., Large-Scale Synthesis of Ultrathin Manganese Oxide Nanoplates and Their Applications to T1 MRI Contrast Agents. *Chem. Mater.* **2011,** *23*, 3318-3324.
(57) Huang, J.; Hou, Y.; Liu, C.; Jing, L.; Ma, T.; Sun, X.; Gao, M., Chemical Spacer Design for Engineering the Relaxometric Properties of Core–Shell Structured Rare Earth Nanoparticles. *Chem. Mater.* **2015,** *27*, 7918-7925.
(58) Zhou, Z.; Huang, D.; Bao, J.; Chen, Q.; Liu, G.; Chen, Z.; Chen, X.; Gao, J., A Synergistically Enhanced T1–T2 Dual-Modal Contrast Agent. *Adv. Mater.* **2012,** *24*, 6223-6228.
(59) Niu, D.; Luo, X.; Li, Y.; Liu, X.; Wang, X.; Shi, J., Manganese-Loaded Dual-Mesoporous Silica Spheres for Efficient T1- and T2-Weighted Dual Mode Magnetic Resonance Imaging. *ACS. Appl. Mater. Inter.* **2013,** *5*, 9942-9948.
(60) Yang, H.; Zhuang, Y.; Sun, Y.; Dai, A.; Shi, X.; Wu, D.; Li, F.; Hu, H.; Yang, S., Targeted dual-contrast T1- and T2-weighted magnetic resonance imaging of tumors using multifunctional gadolinium-labeled superparamagnetic iron oxide nanoparticles. *Biomaterials* **2011,** *32*, 4584-4593.
(61) Bae, K. H.; Kim, Y. B.; Lee, Y.; Hwang, J.; Park, H.; Park, T. G., Bioinspired Synthesis and Characterization of Gadolinium-Labeled Magnetite Nanoparticles for Dual Contrast T1- and T2-Weighted Magnetic Resonance Imaging. *Bioconj. Chem.* **2010,** *21*, 505-512.
(62) Lee, N.; Yoo, D.; Ling, D.; Cho, M. H.; Hyeon, T.; Cheon, J., Iron Oxide Based Nanoparticles for Multimodal Imaging and Magnetoresponsive Therapy. *Chem. Rev.* **2015,** *115*, 10637-89.
(63) Caravan, P., Strategies for increasing the sensitivity of gadolinium based MRI contrast agents. *Chem. Soc. Rev.* **2006,** *35*, 512-523.

(64) Zhang, X.; Blasiak, B.; Marenco, A. J.; Trudel, S.; Tomanek, B.; van Veggel, F. C. J. M., Design and Regulation of NaHoF4 and NaDyF4 Nanoparticles for High-Field Magnetic Resonance Imaging. *Chem. Mater.* **2016,** *28*, 3060-3072.
(65) Huang, J.; Bu, L.; Xie, J.; Chen, K.; Cheng, Z.; Li, X.; Chen, X., Effects of nanoparticle size on cellular uptake and liver MRI with polyvinylpyrrolidone-coated iron oxide nanoparticles. *ACS Nano* **2010,** *4*, 7151-60.
(66) Walkey, C. D.; Chan, W. C., Understanding and controlling the interaction of nanomaterials with proteins in a physiological environment. *Chem. Soc. Rev.* **2012,** *41*, 2780-99.
(67) Mornet, S. p.; Vasseur, S. b.; Grasset, F.; Duguet, E., Magnetic nanoparticle design for medical diagnosis and therapy. *J. Mater. Chem.* **2004,** *14*, 2161.
(68) Levy, M.; Luciani, N.; Alloyeau, D.; Elgrabli, D.; Deveaux, V.; Pechoux, C.; Chat, S.; Wang, G.; Vats, N.; Gendron, F.; Factor, C.; Lotersztajn, S.; Luciani, A.; Wilhelm, C.; Gazeau, F., Long term in vivo biotransformation of iron oxide nanoparticles. *Biomaterials* **2011,** *32*, 3988-3999.
(69) Jain, T. K.; Reddy, M. K.; Morales, M. A.; Leslie-Pelecky, D. L.; Labhasetwar, V., Biodistribution, Clearance, and Biocompatibility of Iron Oxide Magnetic Nanoparticles in Rats. *Mol. Pharm.* **2008,** *5*, 316-327.
(70) Pouliquen, D.; Le Jeune, J. J.; Perdrisot, R.; Ermias, A.; Jallet, P., Iron oxide nanoparticles for use as an MRI contrast agent: Pharmacokinetics and metabolism. *Magn. Reson. Imaging* **1991,** *9*, 275-283.
(71) Cui, J.; Richardson, J. J.; Björnmalm, M.; Faria, M.; Caruso, F., Nanoengineered Templated Polymer Particles: Navigating the Biological Realm. *Acc. Chem. Res.* **2016,** *49*, 1139-1148.
(72) Chouly, C.; Pouliquen, D.; Lucet, I.; Jeune, J. J.; Jallet, P., Development of superparamagnetic nanoparticles for MRI: effect of particle size, charge and surface nature on biodistribution. *J. Microencapsul.* **1996,** *13*, 245-255.
(73) Pérez-Campaña, C.; Gómez-Vallejo, V.; Puigivila, M.; Martín, A.; Calvo-Fernández, T.; Moya, S. E.; Ziolo, R. F.; Reese, T.; Llop, J., Biodistribution of Different Sized Nanoparticles Assessed by Positron Emission Tomography: A General Strategy for Direct Activation of Metal Oxide Particles. *ACS Nano* **2013,** *7*, 3498-3505.
(74) De Jong, W. H.; Hagens, W. I.; Krystek, P.; Burger, M. C.; Sips, A. J. A. M.; Geertsma, R. E., Particle size-dependent organ distribution of gold nanoparticles after intravenous administration. *Biomaterials* **2008,** *29*, 1912-1919.

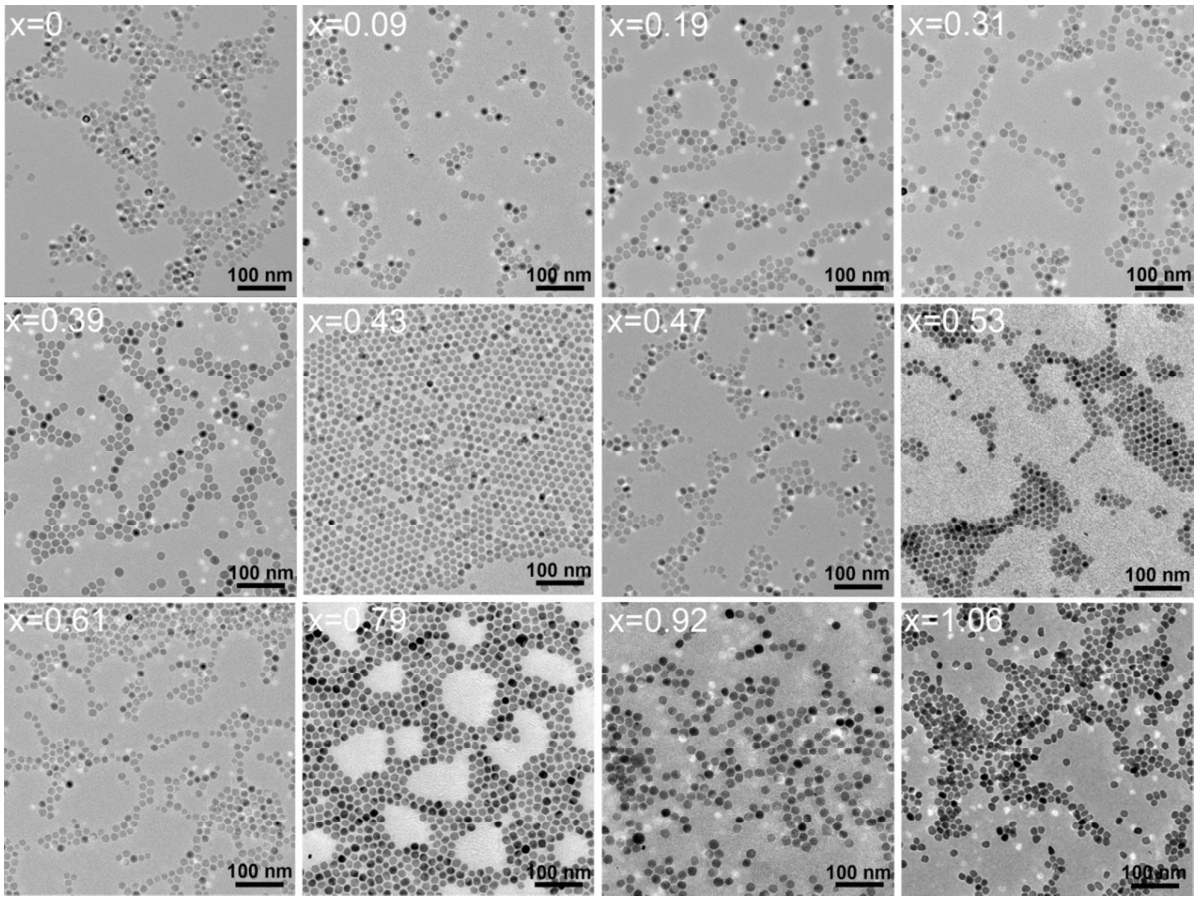

Figure 1. TEM images of Fe_3O_4 (x = 0) and $Mn_xFe_{3-x}O_4$ nanoparticles with various manganese doping levels (x = 0.09, 0.19, 0.31, 0.39, 0.43, 0.47, 0.53, 0.61, 0.79, 0.92, and 1.06). The nanoparticles are spherical shape with narrow size distribution.

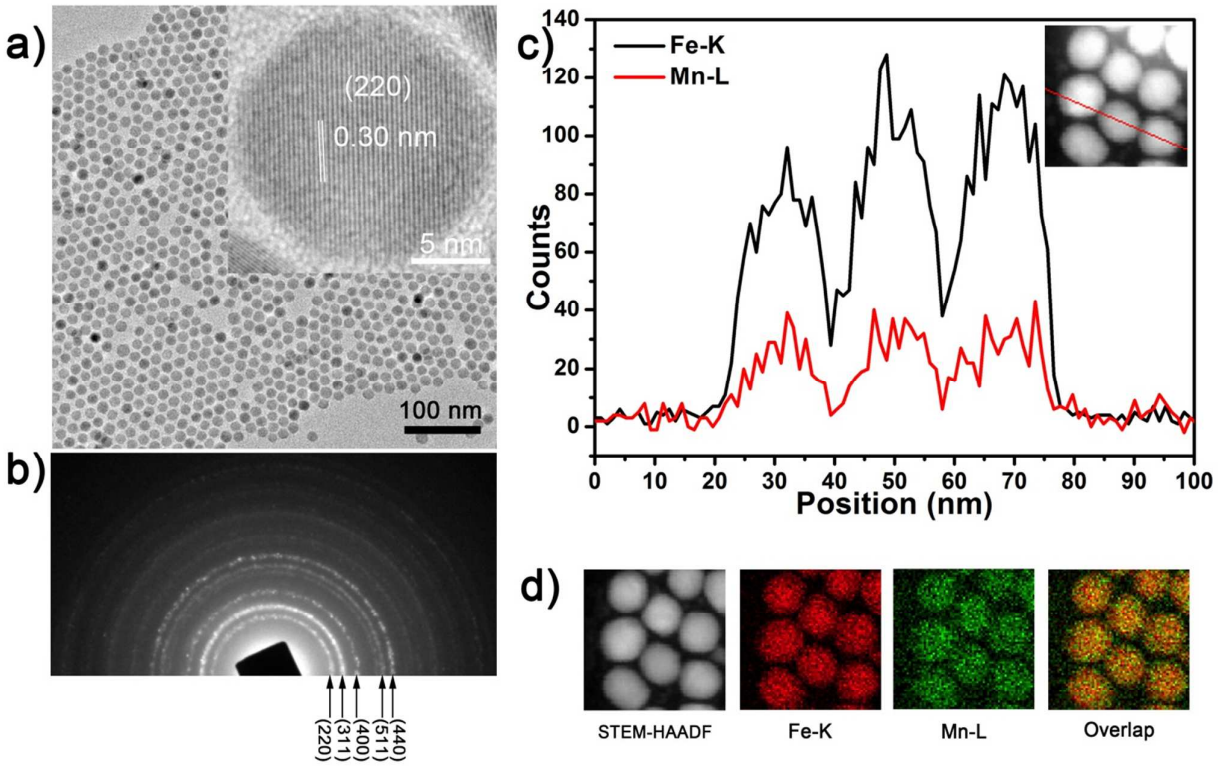

Figure 2. Characterizations of $Mn_xFe_{3-x}O_4$ nanoparticles (x = 0.43). (a) Transmission electron microscopy (TEM) image (inset: HRTEM image), (b) selected area electron diffraction (SAED) patterns, (c) the energy-dispersive X-ray line scanning analysis (EDX) line profiles (inset: STEM-HAADF image), and (d) EDX mapping images of $Mn_xFe_{3-x}O_4$ nanoparticles (x = 0.43).

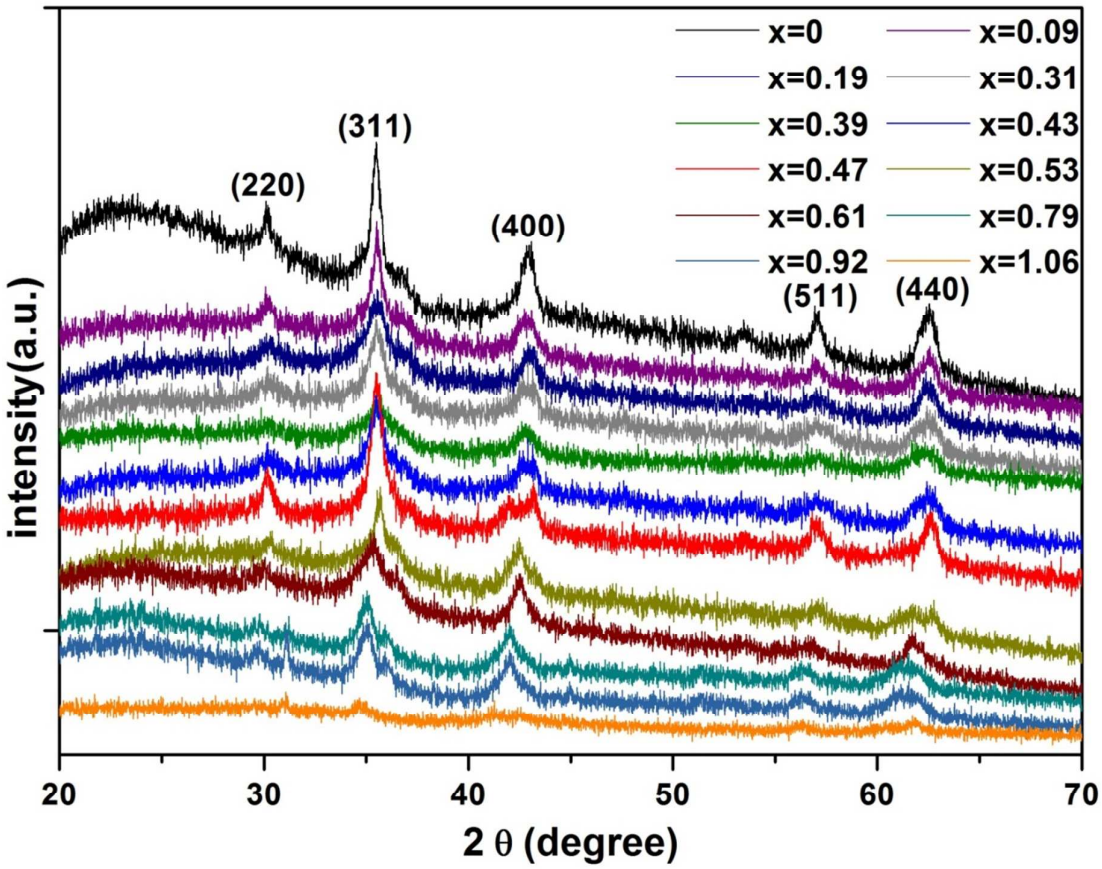

Figure 3. X-ray powder diffraction (XRD) patterns of $Mn_xFe_{3-x}O_4$ nanoparticles with different manganese doping levels. It is noteworthy that the red line was the pattern of $Mn_xFe_{3-x}O_4$ with the manganese doping level of 0.47, from which the shifting of peaks became significant with the increase of manganese doping level.

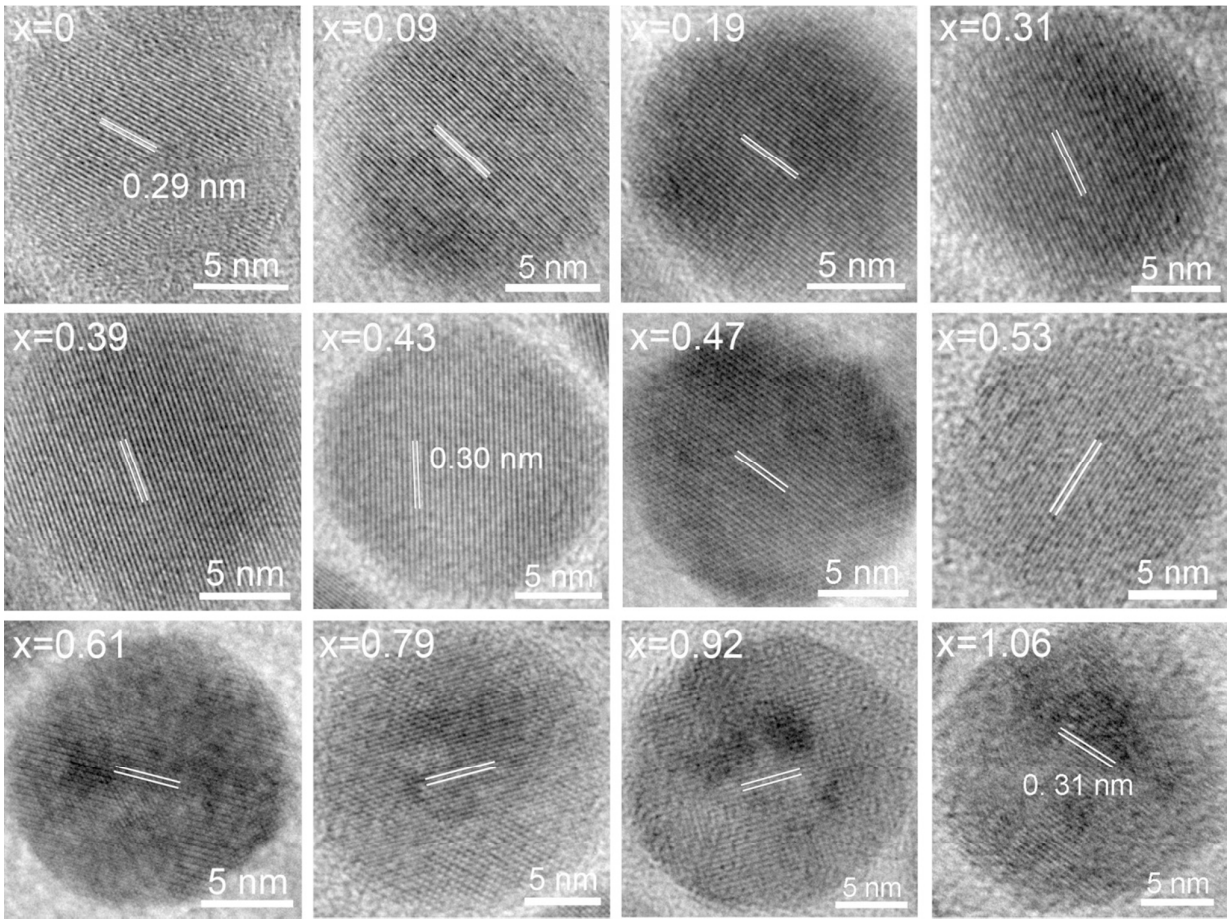

Figure 4. Crystal lattices of (220) in HRTEM images of Fe_3O_4 nanoparticles and $Mn_xFe_{3-x}O_4$ nanoparticles with different manganese doping levels. The (220) lattice distances were increased from 0.29 nm (x = 0, Fe_3O_4) to 0.30 nm (x = 0.43, $Mn_xFe_{3-x}O_4$), and finally is 0.31 nm (x = 1.06, $Mn_xFe_{3-x}O_4$). Meanwhile, the disturbed lattice fringes became significant (after x > 0.43) with the augment of manganese doping level.

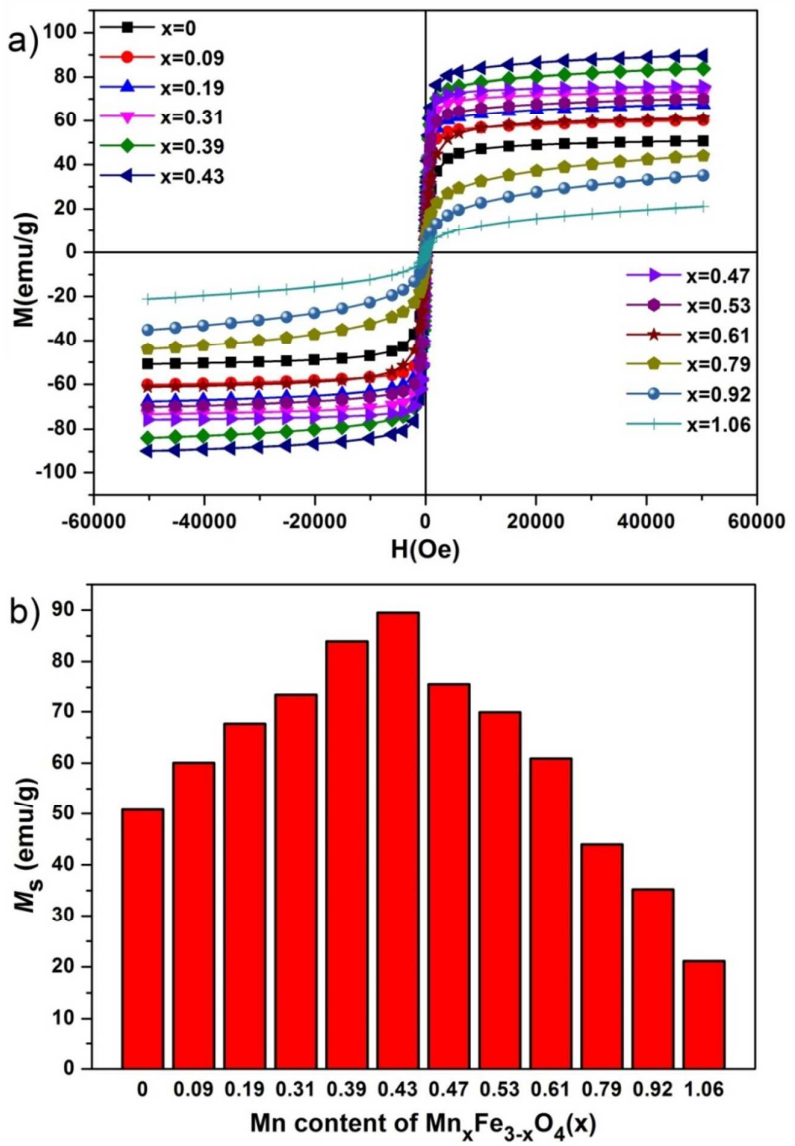

Figure 5. Magnetic properties of $Mn_xFe_{3-x}O_4$ with different manganese doping levels. (a) Field-dependent magnetization curves (*M–H*) of $Mn_xFe_{3-x}O_4$ nanoparticles of various manganese doping levels at 300 K. (b) The comparison of saturated magnetization (M_s) of above mentioned $Mn_xFe_{3-x}O_4$ samples.

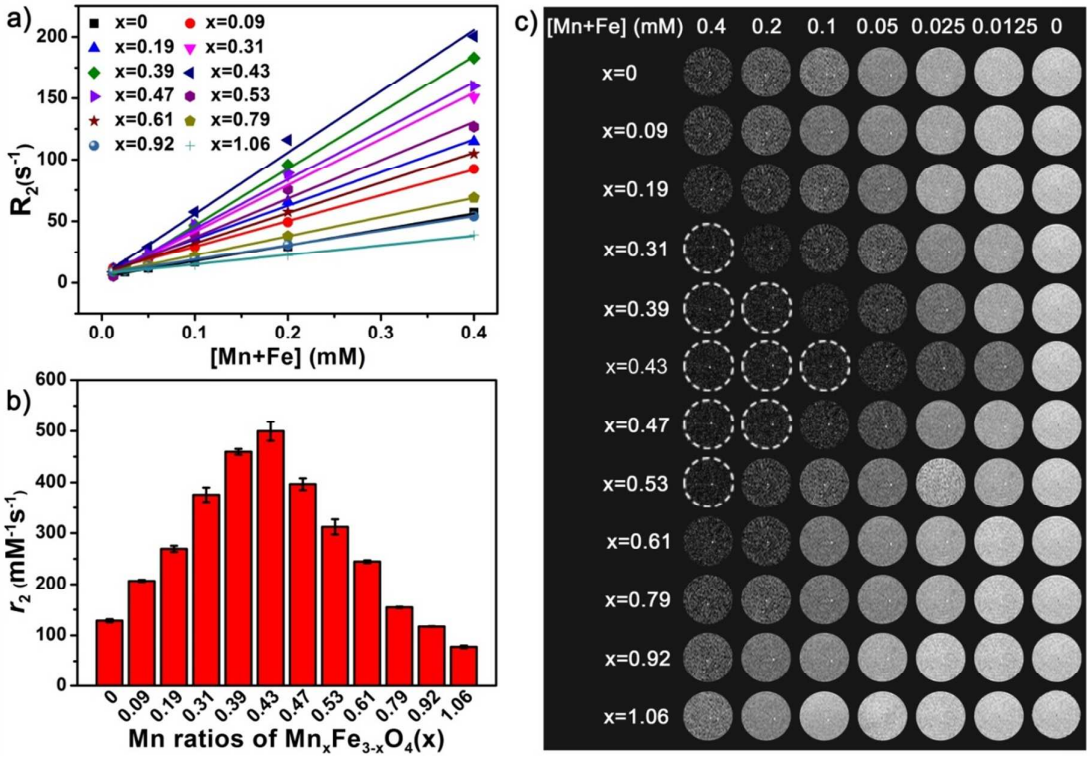

Figure 6. Relaxivity measurements on a 0.5 T scanner. (a) The analysis of relaxation rate R_2 ($1/T_2$). (b) The T_2 relaxivities and (c) T_2-weighted phantom imaging of $Mn_xFe_{3-x}O_4$ nanoparticles with different manganese doping levels, indicating that $Mn_xFe_{3-x}O_4$ nanoparticles with x = 0.43 exhibit the highest T_2 contrast ability among all samples. The relaxivity values r_2 were derived from the slopes of linear fits of experimental data.

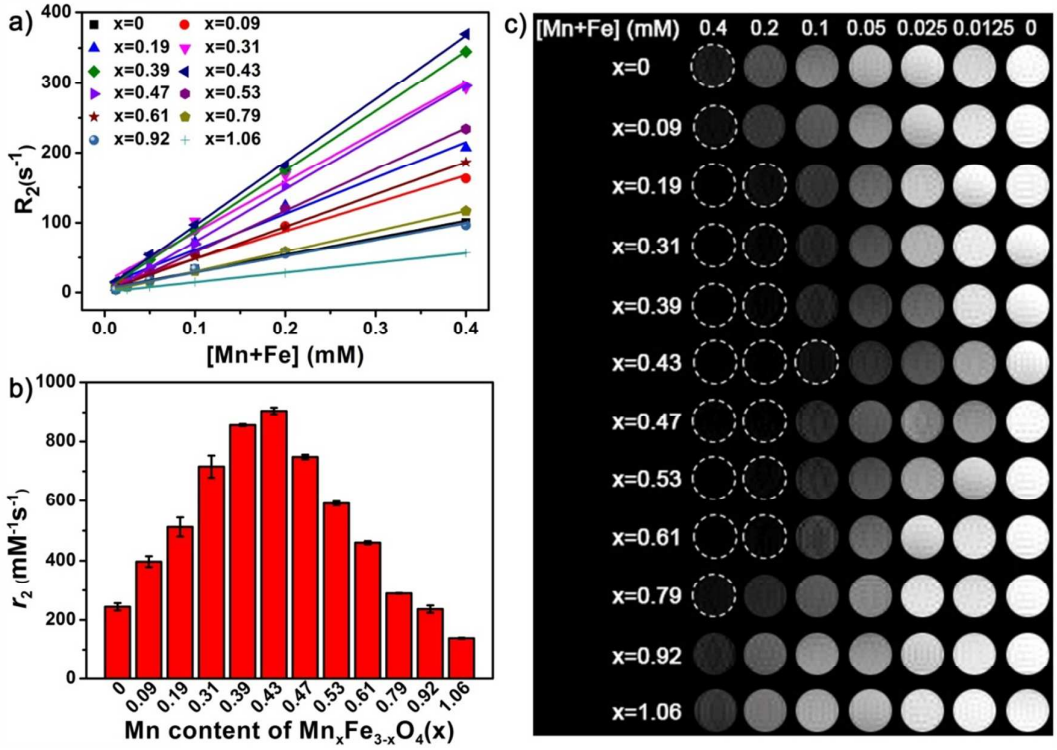

Figure 7. Relaxivity measurements on a 7 T scanner. (a) The analysis of relaxation rate R_2 ($1/T_2$). (b) The T_2 relaxivities and (c) T_2-weighted phantom imaging of $Mn_xFe_{3-x}O_4$ nanoparticles with different manganese doping levels, showing that the r_2 value of $Mn_xFe_{3-x}O_4$ nanoparticles with x = 0.43 is as high as ~904.4 mM^{-1} s^{-1}. The r_2 values were derived from the slopes of linear fits.

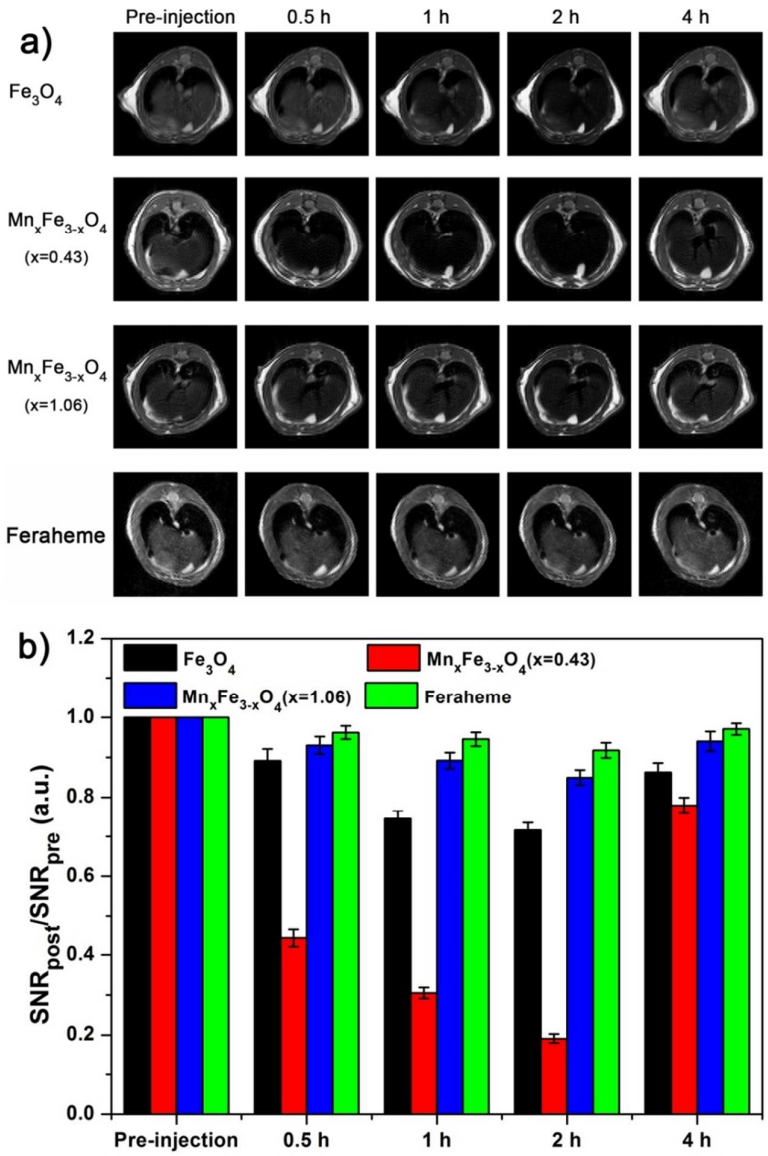

Figure 8. *In vivo* T_2-weighted MR imaging of liver at transverse plane and the related quantitative analysis of signal changes at 7.0 T. (a) T_2-weighted MR images at 0, 0.5, 1, 2 and 4 h post intravenous injection of nanoparticles at a dose of 1 mg [Fe]/kg or 1 mg [Mn + Fe]/kg to mouse body weight. (b) Quantification of signal changes (SNR_{post}/SNR_{pre}) in liver at different time points after administration (n = 3/group).

ToC figure

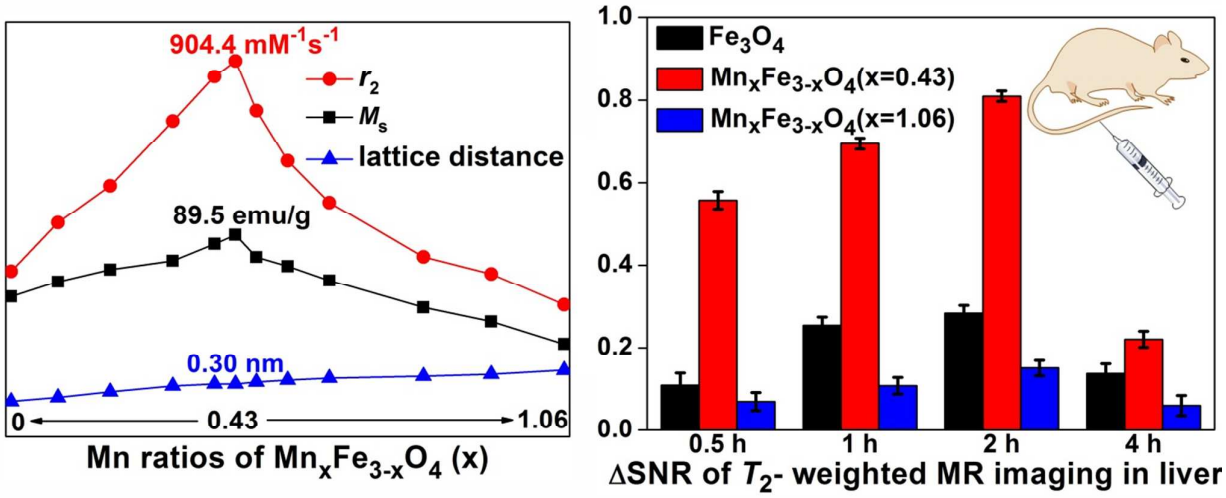
904.4 mM-1s-1
r2
Ms
lattice distance
89.5 emu/g
0.30 nm
0
0.43
1.06
Mn ratios of MnxFe3-xO4 (x)
Fe3O4
MnxFe3-xO4(x=0.43)
MnxFe3-xO4(x=1.06)
1.0
0.8
0.6
0.4
0.2
0.0
0.5 h
1 h
2 h
4 h
ΔSNR of T2- weighted MR imaging in liver